Sequential physical vapor deposited methylammonium lead tri-iodide perovskites on FTO and ITO modified zinc oxide nanorods for perovskite solar cells

M.A. Mayimele, J.N., Fru, J.S. Nyarige and M. Diale

Department of Physics, University of Pretoria, Private Bag X20, Hatfield, 0028, South Africa

*Corresponding author.mmantsae.diale@up.ac.za

Department of Physics, University of Pretoria, Private Bag X20, Hatfield, 0028, South Africa

Abstract

A comparative study was conducted between methylammonium lead tri-iodide ($MAPbI_3$)/zinc oxide (ZnO) nanorods (NRs) on fluorine-doped tin oxide (FTO) and indium tin oxide (ITO) substrates for the first time. X-ray diffraction micrographs confirmed pure tetragonal $MAPbI_3$ phase with I4/mcm space group and highly textured wurtzite hexagonal ZnO structure, having $P6_3mc$ space group. Scanning electron micrographs revealed compact $MAPbI_3$ grains on vertically aligned NRs. The average diameter of the NRs was 226 nm on ITO and 233 nm on FTO. Similarly, the average grain sizes of $MAPbI_3$ were 280 nm and 210 nm on FTO/ZnO and ITO/ZnO, respectively. The bandgaps were respectively 3.05 and 3.18 eV for ITO/ZnO and FTO/ZnO, whereas that of FTO/ZnO/$MAPbI_3$ and FTO/ZnO/$MAPbI_3$ were 1.580 and 1.584 eV, accordingly. Our findings indicate that FTO/ZnO/$MAPbI_3$/Au solar cells have a better performance than ITO/ZnO/$MAPbI_3$/Au devices, and in-chamber annealing did not decompose $MAPbI_3$ sequential vapor-deposited on ZnO nanorods.

Keywords: Zinc oxide nanorods; Methylammonium lead tri-iodide perovskite; Vapor-deposited; Indium tin oxide; Fluorine-doped tin oxide; Solar cells

1. Introduction

Interest in zinc oxide (ZnO) group II-VI semiconductor as an electron transport layer (ETL) in the rapidly growing perovskite solar cells technology is increasing at an accelerated rate [1]. Their high transmittance in the visible region, wide and direct bandgap (3.37 eV), the large exciton binding energy (~60 meV) at room temperature, diversity in morphology, piezoelectric and dielectric nature are desirable properties contributing to the wide range of applications [[2], [3], [4]]. The various morphologies of ZnO implemented in perovskite solar cells to date include nanoparticles/quantum dots [[5], [6], [7]], nanorods (NRs) [8], and nanowires [9]. Perovskites solar cells with ZnO ETL have also been shown to perform better than those with titanium dioxide(TiO_2). *Sun* et al. compared the PCE of solar cells based on ZnO with those based on titanium dioxide (TiO_2) electron transport layer (ETL), both prepared under the same conditions [10]. They observed that the ZnO-based solar cells performed better with a PCE of 17.1% compared to TiO_2 based solar cells with only 12.2% PCE. Besides, *Son* et al. observed that ZnO nanorods are more effective in charge collection than TiO_2 in Methylammonium lead tri-iodide ($MAPbI_3$) perovskite solar cells [11]. $MAPbI_3$ perovskite solar cells using ZnO-NRs as ETL are so far the most efficient of all the solar cells using ZnO nanostructures, with a record power conversion efficiency (PCE) of 17.3% [8].

These results add more guarantee on the promise of ZnO-based perovskite solar cells over the state-of-the-art TiO_2 nanostructured based perovskite solar cells.

However, $MAPbI_3$/ZnO interface is unstable during thermal annealing. Thermal annealing causes degradation $MAPbI_3$ when ZnO is used as ETL [12]. On the contrary, thermal annealing reverses photo-induced degradation of $MAPbI_3$-based solar cells containing nickel oxide (NiO) hole transport layers [13]. The fundamental nature of ZnO surfaces including hydroxyl groups and residual acetate ligands have been shown to cause thermal instability of ZnO-based $MAPbI_3$ perovskite solar cells [5,6]. *Cheng* et al. proved that the basic nature of ZnO causes the deprotonating of the methylammonium cation in $MAPbI_3$ during thermal annealing and this decomposition is accelerated by the presence of hydroxyl groups and acetate ligands on the surface of ZnO [5]. However, the calcination of ZnO at temperatures exceeding 400 °C removed the hydroxyl groups and acetate ligands and produced a more heat-robust perovskite. *Yang* et al. proved that using a poly(ethyleneimine) (PEI) polymeric buffer layer effectively separates the ZnO-nanoparticles and perovskite, allowing larger crystal formation during thermal annealing without decomposition [6]. Using a quasi-core shell structure of ZnO/reduced graphene oxide (rGO) quantum dots as ETL reduces the thermal decomposition during annealing as these (rGO quantum dots) passivates the ZnO nanoparticles and also accelerates charge carrier extraction [14]. This rapid thermal transformation of $MAPbI_3$ to PbI_2 during thermal annealing of $MAPbI_3$ thin films on ZnO surfaces has discouraged the use of one-step preparation methods for $MAPbI_3$ on ZnO [15].

The preparation method, precursor solution, conditions of preparation, and kind of substrates determine the size and shape of the ZnO nanomaterial for the ETL [16] and consequently the PCE of perovskite solar cells. *Ahmadi* et al. changed the morphological, optical, structural, and electrical properties of $MAPbI_3$ by changing the typical solvents used in the preparation of the ZnO nanoparticles ETL including 2-methoxy ethanol, isopropanol, and ethanol [7]. They found that the solar cells using 2-methoxy ethanol had the best PCE because of good surface coverage by $MAPbI_3$, the largest average grain size, and very few pin-holes. *Yun* et al. optimized the lengths of ZnO-NRs by precisely controlling the reaction times and reported a PCE of 14.22% for an optimum length of the ZnO-NRs ETL in $MAPbI_3$ solar cells [17]. The addition of EosinY in solution during the growth of ZnO-NRs increased the diameter of the rods and consequently, the PCE of the solar cell [18]. *Dash* et al. prepared ZnO-NRs on Si (100) wafer using a hydrothermal method and a solution containing zinc nitrate hexahydrate ($Zn(NO_3)_2 \cdot 6H_2O$) and hexamethylenetetramine [19]. They observed 200 nm diameter NRs having a length of 3000 nm. Similarly, *Şahin* et al. prepared ZnO-NRs on ITO substrates using the same solution containing the hydrothermal method and a solution containing zinc nitrate hexahydrate ($Zn(NO_3)_2 \cdot 6H_2O$) and hexamethylenetetramine. Still, they obtained a diameter of 100 nm and a length of 1650 nm [20]. *Slimani* et al. prepared ZnO-NRs on FTO by spray pyrolysis using a solution containing zinc acetate dehydrated ($Zn(CH_3COO)_2 \cdot 2H_2O$) and sodium hydroxide (NaOH) and obtained a diameter of 240 nm and length of 670 nm [16]. *Hari* et al. prepared open and closed hexagonal ZnO-NRs on ITO by chemical bath deposition (CBD) using equimolar amounts of Zn $(NO_3)_2 \cdot 6H_2O$ and hexamethylenetetramine for varying deposition times [21]. They found that the NRs grown when the temperature of the bath was set at 95 °C for 4 h had mainly open ends while the ratio of the area of open NRs to closed NRs decreased as chemical bath time was increased from values exceeding 9 h. *Mwankemwa* et al..showed that the orientation of seed the layer in a growth solution during CBD of ZnO determines the morphology and optical properties and vertically aligned nanorods are grown when the seed layer is facing downwards [22]. *Kumar* et al. studied the difference in the performance of $MAPbI_3$ solar cells using ZnO-NRs on

FTO, and flexible ITO coated polyethylene terephthalate (PET) substrates [23]. They observed that the solar cells on FTO resulted in a PCE of 8.90% while those on ITO/PET showed a PCE of 2.62%. Besides, they also showed that solar cells containing compact ZnO produced by electro-deposition were less efficient than solar cells fabricated with chemical bath deposited ZnO-NRs. To the best of our knowledge, a comparative study of ZnO-NRs ETL grown in CBD on the commonly used glass/FTO and glass/ITO for vapor deposited $MAPbI_3$ cells is yet to be conducted.

In this article, we performed a comparative study of ZnO nanorods ETL synthesized on FTO, ITO, and microscopic glass substrates using CBD, for application in $MAPbI_3$ perovskite solar cells. Non-post-annealed $MAPbI_3$ perovskites were prepared on the ZnO-NRs using a sequential physical vapor deposition approach, previously reported by *Fru* et al. [24,25]. Changes in the structural, morphological, and optical properties of FTO/ZnO, ITO/ZnO, glass/ZnO, FTO/ZnO/$MAPbI_3$, ITO/ZnO/$MAPbI_3$, and glass ZnO/$MAPbI_3$ layers were studied. The dark current-voltage characteristics of FTO/ZnO/$MAPbI_3$/Au and ITO/ZnO/$MAPbI_3$/Au Schottky diodes were compared with those of glass/FTO/ZnO/Au and ITO/ZnO/Au, and ideality factor, reverse saturation currents, series resistances and Schottky barrier height computed for each device. Besides, hole-transport-layer free solar cells on FTO and ITO were fabricated and their performances compared. This study opens new doors to low-cost, stable, and efficient vapor deposited hole-transport layer-free perovskites solar cells including $MAPbI_3$ on ZnO.

2. Experimental

2.1. Growth of ZnO-NRs using chemical bath deposition (CBD)

Fig. 1 is the schematic diagram for the synthesis of ZnO-NRs on various substrates by CBD. Indium tin oxide (ITO), Fluorine-doped tin oxide (FTO), and microscopic glass substrates under test were cleaned with a warm soap solution and rinsed using deionized (DI) water. The substrates were ultra-sonicated for 5.0 min each using acetone, ethanol, and DI water. The sol-gel was first prepared by dissolving an appropriate amount of zinc acetate dihydrate ($Zn(CH_3COO)_2 \cdot 2H_2O$; Sigma) in 25 ml of ethanol, and 40 mM monoethanolamide added to the solution and then overnighted. The cleaned ITO was partly covered with a non-sticking heat resistant tape and sol-gel spin-coated at 3000 rpm for 1.0 min to form a ZnO seed layer which was dried in an oven at 150 °C. The process was repeated 3 times to increase the thickness of the seed layer. The seed layer was then annealed at 350 °C for 1.0 h. 50 mM zinc nitrate hexahydrate ($Zn(NO_3)_2 \cdot 6H_2O$; Sigma) and 50 mM hexamethylenetetramine were dissolved in equimolar amounts in DI water. For all the constituents to completely dissolve, the mixtures were stirred for 1.0 h at room temperature. Nylon cable ties were used to suspend the substrates, with the seeded surface facing down, in a beaker containing the growth solution. This was done to ensure the vertical growth of NRs on the seeded layer. The growth solution was then placed inside a water bath at a temperature of 90 °C, which was maintained throughout the experiment. After 4 h, the synthesized ZnO-NRs samples were washed with DI water, dried with pressurized nitrogen flow, and then annealed at 400 °C for 30 min.

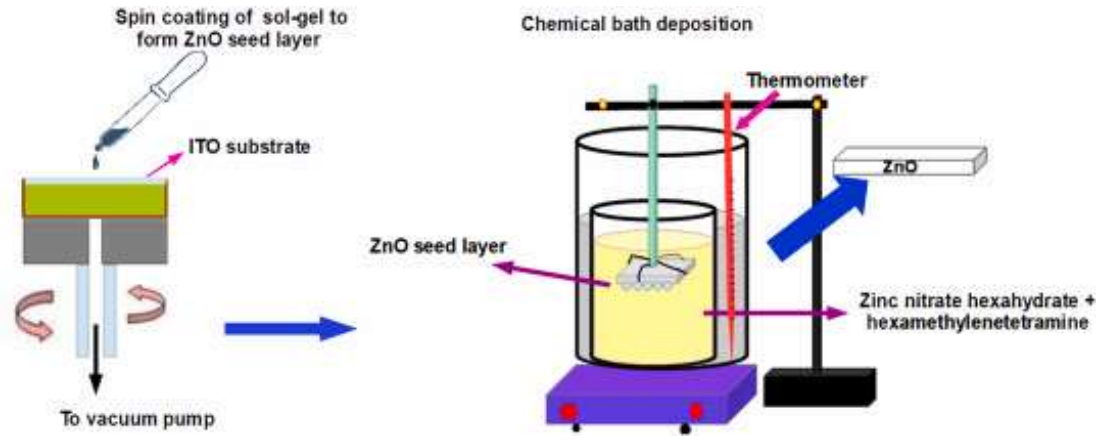

Fig. 1. The schematic diagram for growth of ZnO-NRs on ITO substrate.

2.2. The growth of $MAPbI_3$ on ZnO-NRs by sequential physical vapor deposition (SPVD)

Fig. 2(a) shows the schematics for the growth of 3D $MAPbI_3$ perovskite thin films on ZnO substrate using SPVD previously optimized by *Fru* et al. [24]. The ZnO substrate was loaded into the evaporation chamber containing lead (II) iodide (PbI_2) and methylammonium iodide (MAI) in two separate boron nitride crucibles. Air was pumped out of the chamber until a suitable vacuum (2.0×10^{-5} mbars) was attained. 100 nm of PbI_2 was first evaporated by the heat energy generated after a suitable current was applied through the coils surrounding the crucible. The evaporation of 400 nm MAI followed this. An inbuilt quartz crystal monitor was used to monitor the thickness of thin films during the deposition process. The PbI_2 thickness was measured by setting the density of the monitor to 6.16 g cm^{-3} and Z-factor to 1.10 whereas MAI density was set to 1.20 g cm^{-3} and Z-factor to 2.70. The sample was removed from the chamber and annealed at 100 °C for 10 min in air. 100 nm thick gold electrodes were then evaporated onto the $MAPbI_3$ thin films to form a hole transport layer-free device, as shown in Fig. 2(b).

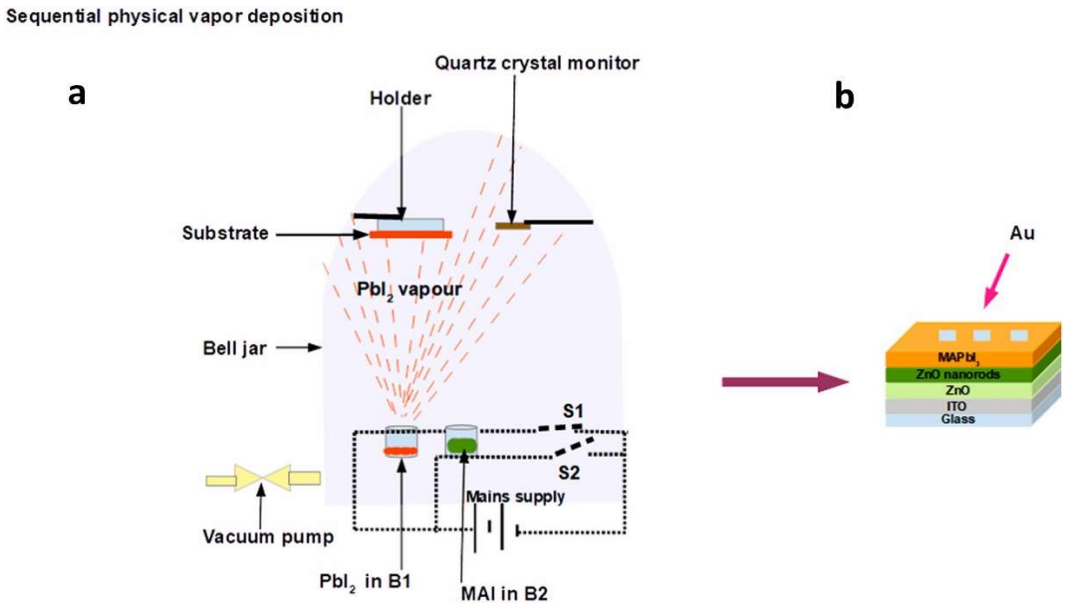

Fig. 2. The schematic diagram for deposition of $MAPbI_3$ and Au Schottky diodes (a) sequential physical vapor deposition of $MAPbI_3$ (b) architecture of Schottky diodes.

The diffractograms of the thin films were determined using a Bruker D2-Phaser X-ray diffract meter having a Cu Kα radiation with a wavelength of 1.5405 Å. The 2Θ angle between the incident and diffracted X-ray beams was varied from 20 to 60° with a scanning rate of $0.05°s^{-1}$. The morphological properties were revealed by a field emission scanning electron microscope (FE-SEM Zeiss Crossbeam 540), with an accelerating voltage of 2.0 kV. The dimensions of the NRs were determined from the FE-SEM images using the ImageJ software. The optical absorption spectra of the films were measured by Agilent CARY 60 UV–Vis spectrometer with the wavelength of incident light in the 400–800 nm range.

2.3. Fabrication of solar cells and Schottky diodes

Schottky diodes and solar cells were fabricated on FTO (~7 Ω/sq, Sigma Aldrich) and ITO (8–12 Ω/sq, Sigma Aldrich) substrates. The FTO and ITO substrates for the solar cells were trimmed to 20 × 15 mm and patterned by etching with concentrated hydrochloric acid and zinc powder. Un-patterned substrates were used for the Schottky diode fabrication. The substrates were cleaned by sequential sonication for 10 min in acetone, ethanol, and DI water and dried with a pressurized flow of pure nitrogen. Both ends of the cleaned patterned substrates were covered using heat-resistant tape before the deposition of the ZnO-NRs ETL. The ZnO-NRs were grown on the substrates using CBD as described above. This was immediately followed by the deposition of the $MAPbI_3$ active layer on the ZnO-NRs using SPVD. The heat-resistant tapes were removed from both ends and gold contacts were deposited via the S211 multi-electrode mask (Ossila). The Schottky diodes were fabricated on the un-patterned 15 mm × 10 mm FTO and ITO substrates following similar steps. However, only one end was covered with heat-resistant tape and a circular mask, 0.6 mm in diameter, was used for the gold contact deposition.

The dark current-voltage (*I–V*) characteristics and device parameters of the Schottky diodes were determined by an automatic set-up placed inside a Faraday cage. The Faraday cage creates darkness and minimizes electrical noise during measurement. The set-up uses a Hewlett Packard pA/DC voltage 4140B source meter, which measures current down to 10^{-15} A with 0.5% accuracy, is used to source *V* and measure the resulting *I*. Current density-voltage (*J-V*) characteristics and device performance parameters of the solar cells under illumination were determined using the automatic *I–V* measurement system (Ossila). The light measurements were performed under a solar simulator (Oriel LCS-100™ Small Area So11A Series, Newport) with simulated solar output conditions of 100 mW/cm^2 and AM1.5 G reference spectral filtering.

3. Results and discussion

3.1. Structural properties

Fig. 3(a-c) shows the diffractograms of ZnO-NRs on various substrates. All the diffractograms showed strong and sharp peaks that matched the stable ZnO wurtzite hexagonal crystal structure with the $P6_3mc$ space group according to JCPDS PDF card number 36–1451 [26]. The intensities of the (002) planes differed significantly from those of the (001), (101), and (102) planes, indicating high texturing with preferred orientation on the (002) plane [27]. This means that the ZnO-NRs tend to grow more on the (002) plane. *Solís-Pomar* et al. [3] explained that the preferential direction in the normal *c*-axes is due to the decomposition of diethylzinc on the substrates to provide nucleation sites for the growth of vertical NRs. The texturing of ZnO-NRs has been shown previously to depend on the time to

grow the seed layer [4] and the orientation of the seed layer along the *c*-axis [28]. Our results show that texting is independent of the kind of substrates on which the seed layer and NRs are grown. The area under the (002) diffraction plane, which is generally taken to be synonymous to the peak intensity, is observed to be highest for FTO as shown in Table 1, implying the highest crystallinity. Fig. 3(d) indicates that ZnO-NRs on FTO and ITO are more crystalline than on glass. This is because the (002) peak of ZnO-NRs grown on FTO and ITO are more intense than that of ZnO grown on glass. The high peak intensity could be due to a more significant number of the (002) refection planes on FTO and ITO, which increases the multiplicity factor.

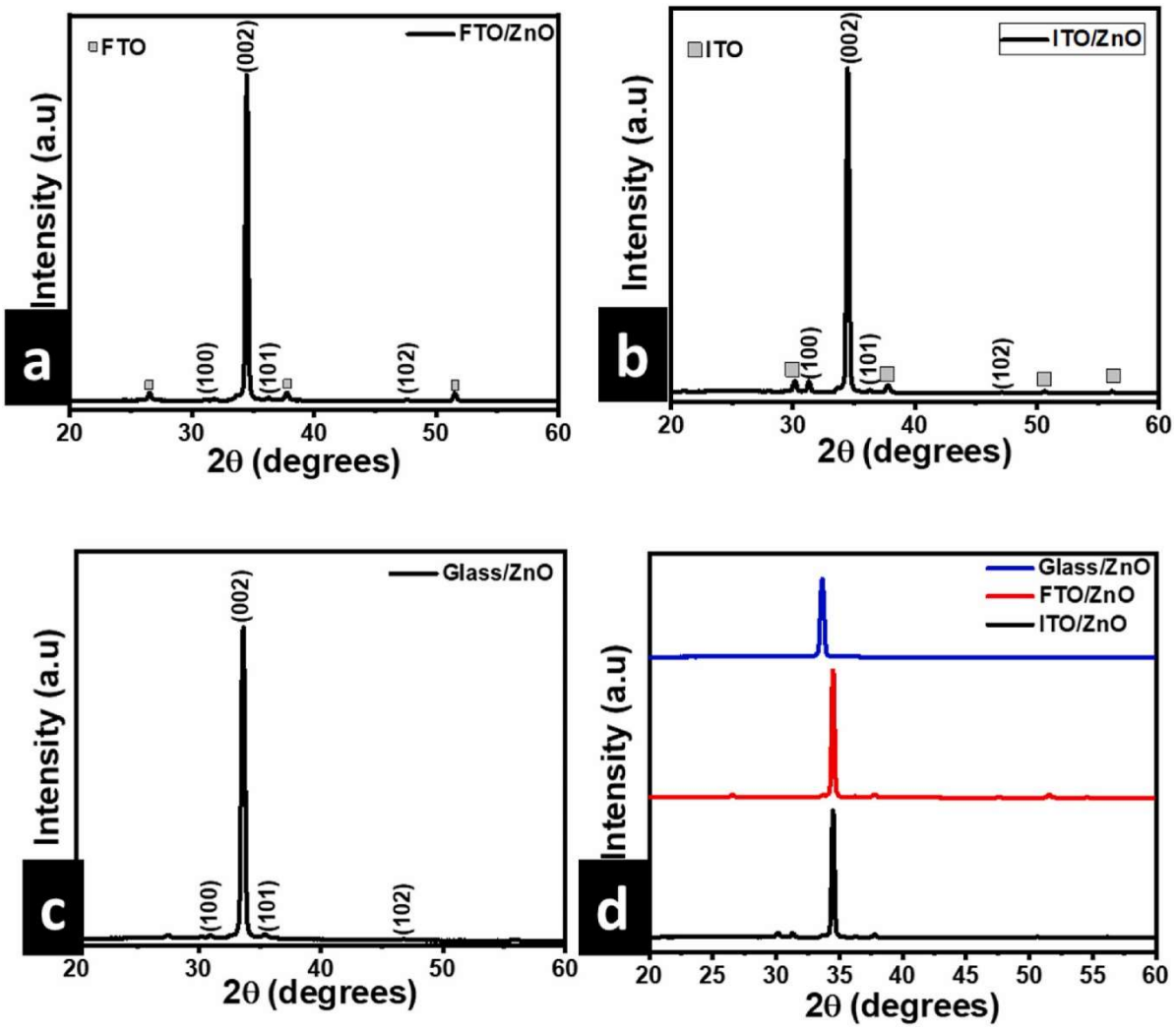

Fig. 3. Diffractograms of ZnO-NRs on various (a) ZnO-NRs on FTO (b) ZnO-NRs on ITO substrate (c) ZnO-NRs on glass and (d) comparison of peak intensities of the three substrates.

Table 1. Lattice parameters, average crystallite size, and micro-strain of ZnO on various substrates.

ZnO on various types of substrates	The lattice parameter, *a* (Å)	The lattice parameter, *c* (Å)	The average crystallite size (nm)	(002) peak intensity (a.u)	Micro-strain
ITO/ZnO	3.244	5.199	26.56	121005.79	5.07×10^{-4}
FTO/ZnO	3.245	5.189	34.00	121097.57	3.89×10^{-4}
Glass/ZnO	3.319	5.295	25.09	100422.21	5.14×10^{-4}

Fig. 4(a-c) shows the XRD images of the $MAPbI_3$ grown ITO/ZnO, FTO/ZnO, and glass/ZnO substrates, respectively. All the diffractograms confirmed the tetragonal crystal structure of $MAPbI_3$ for all samples, having the I4/mcm space group, consistent with earlier results [24,[29], [30], [31]]. It is important to note that no peaks corresponding to PbI_2 were observed, although thermal annealing occurred within the chamber, unlike for solution deposited $MAPbI_3$ thin films on ZnO in which case thermal decomposition occurs. This means that sequential physical vapor deposited $MAPbI_3$ thin-films on ZnO is stable to annealing within the deposition chamber. In Fig. 4 (c), all the peaks of $MAPbI_3$ on the glass substrate are shifted to angular positions in comparison to peaks on FTO and ITO substrates. This is because the height of the sample on glass is different from that on FTO and ITO. Fig. 4 (d) confirms the uniform shift of all the peaks of the sample on the glass substrates to the left of those on FTO and ITO. A similar difference in peak position was observed in the XRD of powdered and single crystals of the same material by *Jesche* et al. [32].

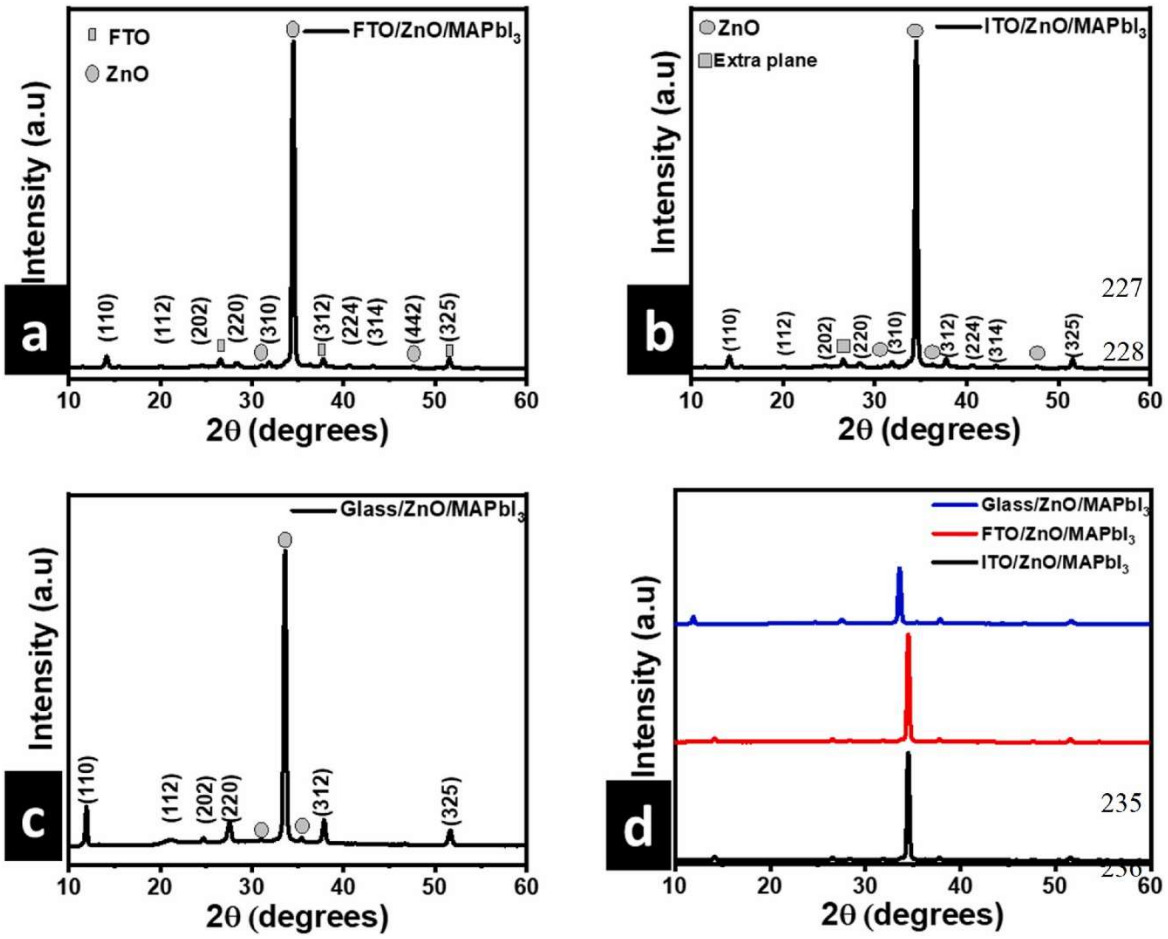

Fig. 4. Diffractograms of ZnO-NRs/$MAPbI_3$ on various substrates (a) ZnO-NRs/$MAPbI_3$ on FTO (b) ZnO-NRs/$MAPbI_3$ on ITO (c) ZnO-NRs/$MAPbI_3$ on glass and (d) comparison of peak intensities of the three substrates.

The highly intense ZnO peaks are also observed alongside those of the $MAPbI_3$. This means that the X-rays are capable of penetrating the $MAPbI_3$ thin film to the ZnO-NRs during the coherent scattering process. The large difference in intensities points to the fact that $MAPbI_3$ film could be thinner than ZnO. Also, it could indicate that ZnO is more crystalline than $MAPbI_3$. The intensity of the (110) peak for $MAPbI_3$ is highest in the ITO substrate (Fig.

4(d)), implying that the $MAPbI_3$ film could be more crystalline on ITO/ZnO and FTO/ZnO than on glass/ZnO.

The crystallite sizes and micro-strains were computed using the Debye-Scherer [33] and the Stokes and Wilson relations [34] given by Eqs. (1), (2), respectively,

$$D = \frac{k\lambda}{\beta \cos \theta} \tag{1}$$

$$\varepsilon = \frac{\beta}{4 \tan \theta} \tag{2}$$

where D is the average crystallite size, λ is the wavelength, β is the full width at half maximum, θ is the Bragg's diffraction angle, ε is the micro-strain and k is a constant determined by the shape of the crystallite and considered to be 0.94. The lattice constants for wurtzite hexagonal crystal structure for ZnO-NRs and the tetragonal structure for $MAPbI_3$ were calculated using **Eq.** 3 and **Eq.** 4, respectively,

$$\frac{1}{d^2} = \frac{4}{3}\left(\frac{h^2+hk+k^2}{a^2}\right) + \frac{l^2}{c^2} \tag{3}$$

$$\frac{1}{d^2} = \frac{h^2+k^2}{a^2} + \frac{l^2}{c^2} \tag{4}$$

where d is the inter-planar spacing, h, k and l are the Miller Indices, and a and c are lattice constants. Table 1 displays the lattice constants, average crystallite size, and micro-strain of the ZnO-NRs. The lattice constant a is comparable for ZnO-NRs on FTO and ITO. However, there is a slight elongation along the c-axis for the sample on ITO. On the other hand, the lattice constants a and c for ZnO on the glass are greater than for ITO and FTO. Generally, there is a positive correlation between the c and the micro-strain. This means that the elongation along the c-axis could be due to an increase in tensile stresses that cause an increase in micro-strain. Table 2 displays the lattice constants, average crystallite size, and micro-strain of the $MAPbI_3$ thin films on ZnO-NRs. Our previous report on the lattice constants when $MAPbI_3$ was prepared on glass under the same conditions gave a as 8.905 Å and c as 12.526 Å [24]. The growth of $MAPbI_3$ thin films on ZnO-NRs caused an elongation along the c-axis and a contraction along the a-axis by comparing the values in Table 2 with the values above previously reported. This change correlates positively with the corresponding lattices constants of ZnO shown in Table 1. This indicates that the difference in the lattice constants is determined by the dimensions of the ZnO unit cells.

Table 2. Lattice parameters, average crystallite size, and microstrain of $MAPbI_3$ on ZnO ground on various substrates.

ZnO on various types of substrates	The lattice parameter, a (Å)	The lattice parameter, c (Å)	The average crystallite size (nm)	Micro-strain
ITO/ZnO/$MAPbI_3$	8.588	13.103	22.45	5.04×10^{-4}
FTO/ZnO/$MAPbI_3$	8.588	13.103	22.55	5.01×10^{-4}
Glass/ZnO/$MAPbI_3$	8.758	12.766	24.80	4.90×10^{-4}

3.2. Morphological properties of $MAPbI_3$

Fig. 5(a-d) shows FE-SEM images of ZnO-NRs on FTO, ITO, and glass substrates. The vertically aligned NRs with hexagonal geometry having variable diameters are observed on

all substrates, confirming the XRD results. The average diameters of the NRs are observed to be 226 ± 23, 233 ± 32, and 169 ± 35 nm on ITO, FTO, and glass substrates, respectively. From the observation of the diameters, the values for the NRs on ITO and FTO are comparable but greater than the average diameter of the NRs on glass. The average length of the ZnO-NRs grown on ITO and FTO as estimated using ImageJ was obtained as 511 ± 34 and 692 ± 25 nm, respectively. However, the length of the NRs on a bare glass substrate was quite different from the ITO and FTO samples. The growth of the ZnO-NRs on ITO, FTO, and glass, are observed to be densely and uniformly distributed on the entire substrate. Comparing Fig. 5(a) and (b), we observed that the NRs were more compact on glass than FTO. It is worth noting that the seed layer of ZnO aided in the nucleation and growth of these NRs.

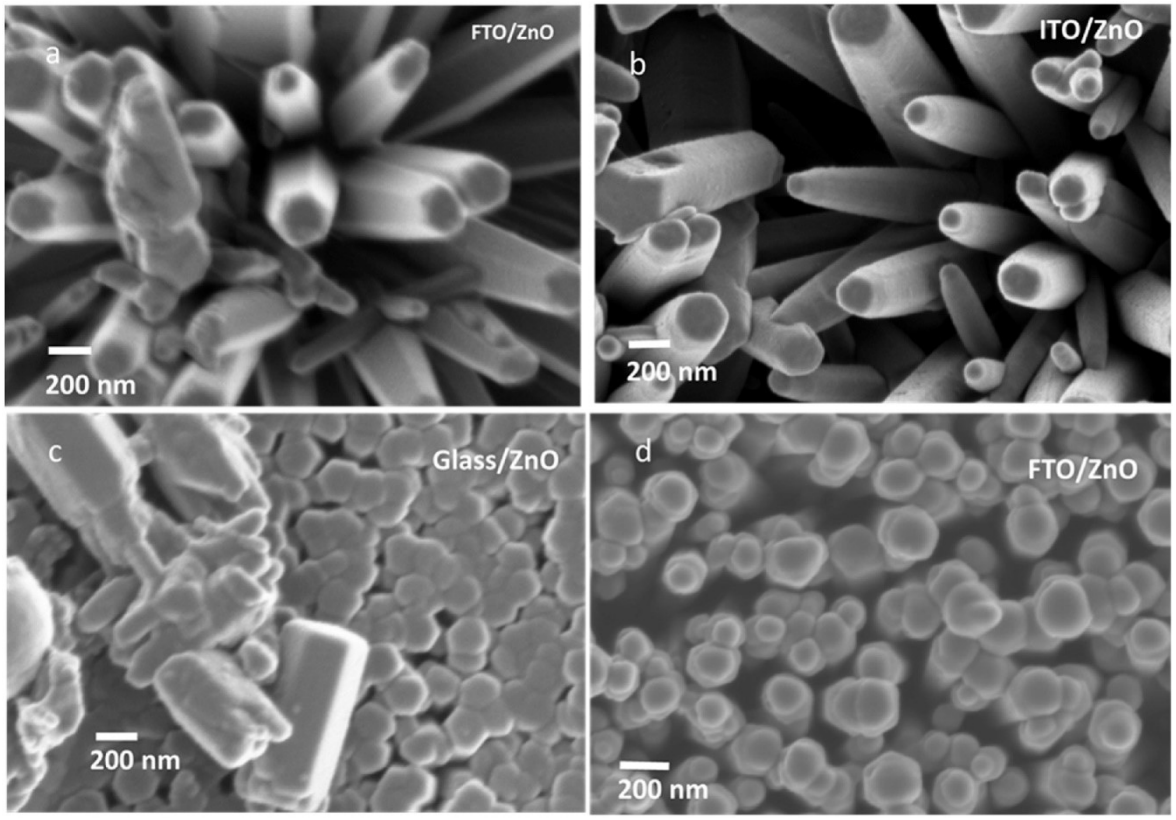

Fig. 5. FE-SEM micrographs of ZnO-NRs on various substrates (a) ZnO-NRs on FTO substrate (b) ZnO-NRs on ITO (c) ZnO-NRs on glass and (d) Top surfaces view of ZnO-NRs on FTO.

Fig. 6(a–d) presents the $MAPbI_3$ grown on as-prepared ZnO-NRs. From the images obtained, the compact $MAPbI_3$ cuboidal grains could be seen on the FTO, ITO, and glass substrates. The $MAPbI_3$ layer entirely covered the ZnO-NRs. Fig. 6(d) shows that the $MAPbI_3$ grains on the faces and also grew along the *c*-axis of the NRs. The grains are observed to be more compact on glass than on FTO and ITO. The compact nature of the $MAPbI_3$ grains is consistent with that of the ZnO-NRs, indicating that the density of the ZnO bottom layer determines how compact the $MAPbI_3$ layer is. The average grain sizes of the $MAPbI_3$ thin films were observed to be 280 ± 39, 210 ± 42, and 173 ± 19 nm on FTO, ITO, and glass substrates, respectively.

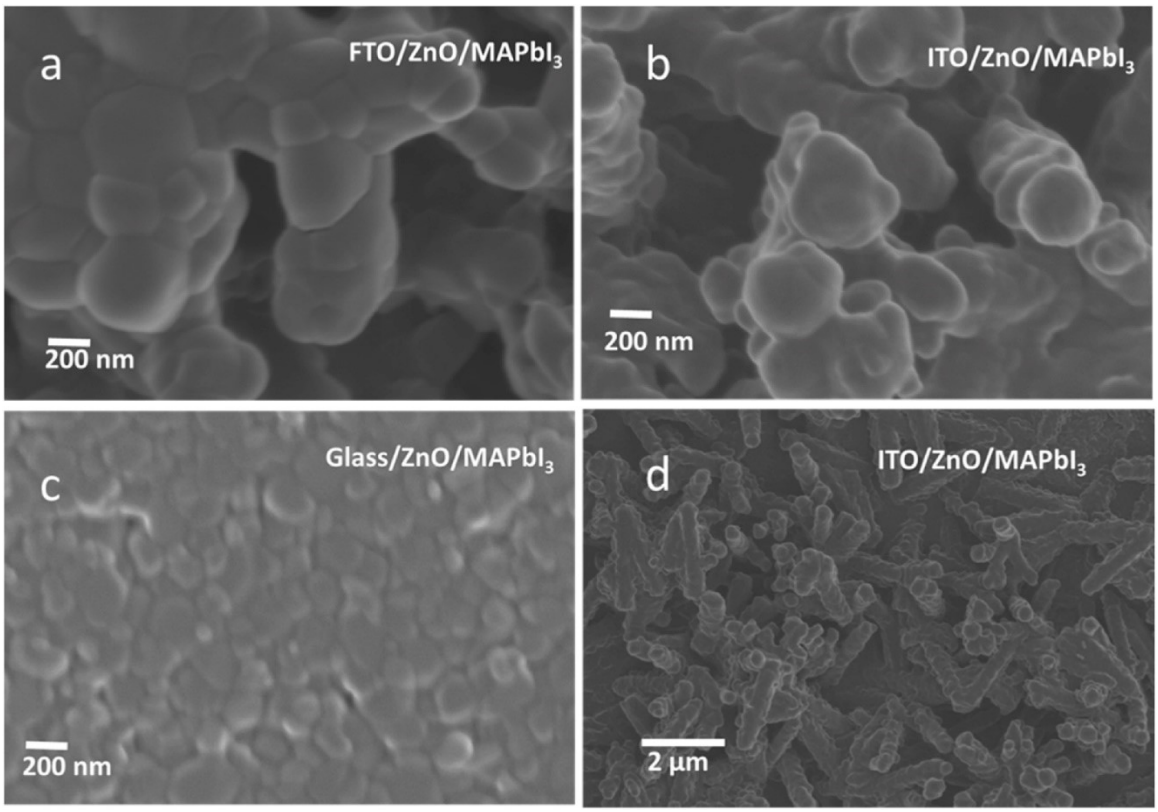

Fig. 6. FE-SEM of ZnO-NRs/$MAPbI_3$ on various substrates (a) ZnO-NRs/$MAPbI_3$ on FTO substrate (b) ZnO-NRs/$MAPbI_3$ on ITO (c) ZnO-NRs/$MAPbI_3$ on a glass and (d) ZnO-NRs/$MAPbI_3$ on ITO.

3.3. Optical properties

Fig. 7(a-d) shows the UV–Vis absorption spectra for ZnO-NRs and $MAPbI_3$ on various substrates. All the spectra for ZnO-NRs on FTO, ITO, and microscope glass substrates show negligible absorbance in the entire visible region and absorption onsets near 380 nm as shown in Fig. 7(a–c), consistent with a previous study [35]. This indicates that the NRs are highly transparent and will transmit most of the visible light to the perovskite absorber for charge carrier generation. Comparing the absorption intensities of the NRs on the different substrates as shown in Fig. 8(a), we observe that the absorbance of the NRs is the same in the visible region but varies significantly in the ultraviolet region. Besides, the absorption edges of the spectra are very sharp, indicating the absence of deep-level defects in the ZnO-NRs [36]. ITO/ZnO absorbs more the visible region than FTO/ZnO. This could be because ITO loses its transparency when annealed at high temperatures exceeding 300 °C [37]. We confirm that $MAPbI_3$ is present on ZnO from the visible absorption spectra. All the spectra of $MAPbI_3$ on ZnO show an absorption onset at 780 nm, in good agreement with previous reports [24,38]. Fig. 7(d*)* compares the spectrum of $MAPbI_3$ on FTO/ZnO, ITO/ZnO, glass/ZnO, and glass. We observe that the spectra differ significantly in the 300–600 nm range and the differences can be related to the compact nature of the $MAPbI_3$, which is also determined by the compact nature of the $MAPbI_3$ on the substrate. It is observed that glass/ZnO/$MAPbI_3$ has the highest absorption intensity while ITO/ZnO/$MAPbI_3$ has the least intensity in this region.

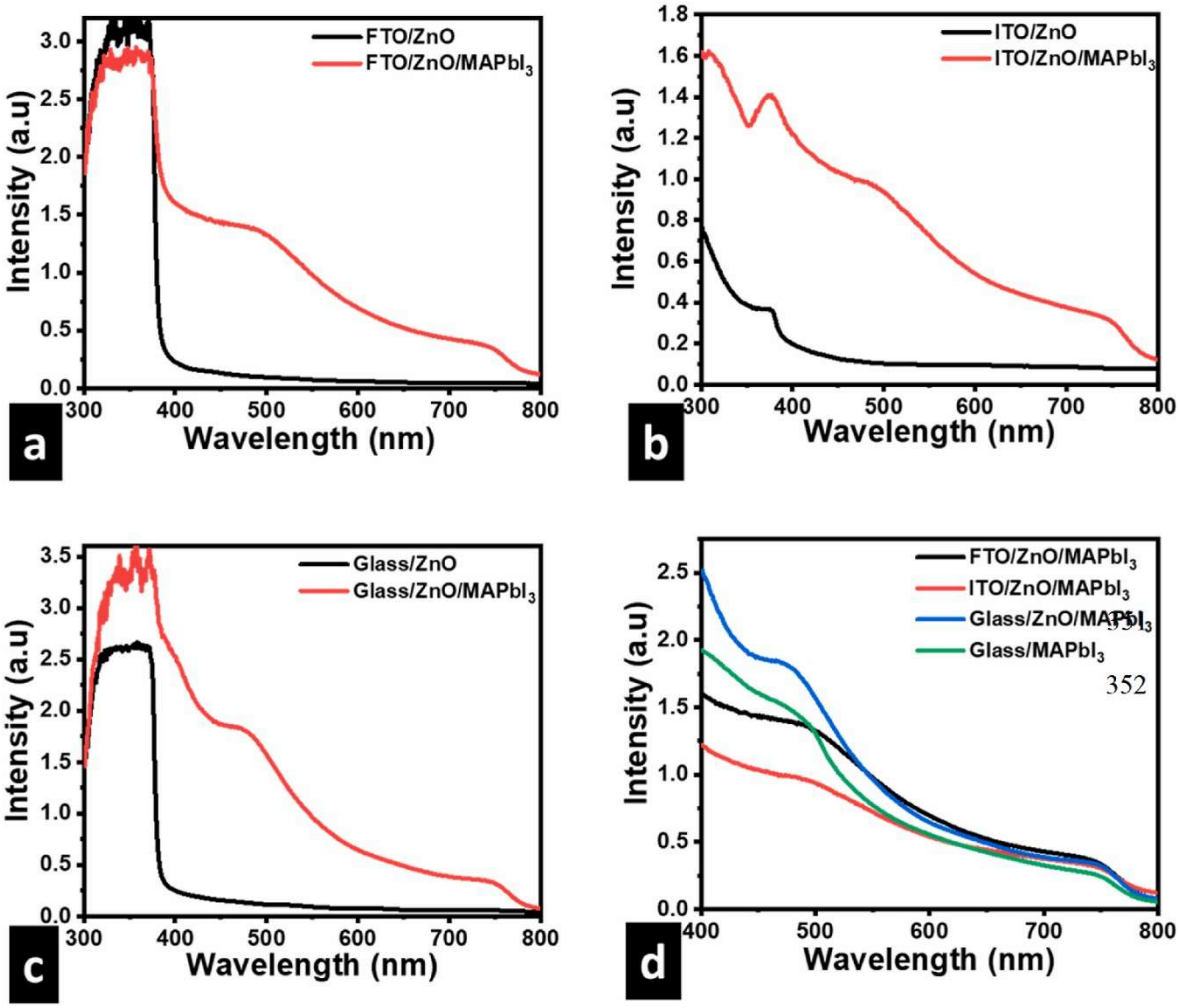

Fig. 7. The absorption spectrum of ZnO-NRs and $MAPbI_3$ on various substrates (a) ZnO on FTO and $MAPbI_3$ on FTO/ZnO (b) ZnO on ITO and $MAPbI_3$ on ITO/ZnO (c) ZnO on glass and $MAPbI_3$ on glass/ZnO (d) $MAPbI_3$ on FTO/ZnO, ITO/ZnO, glass/ZnO, and glass.

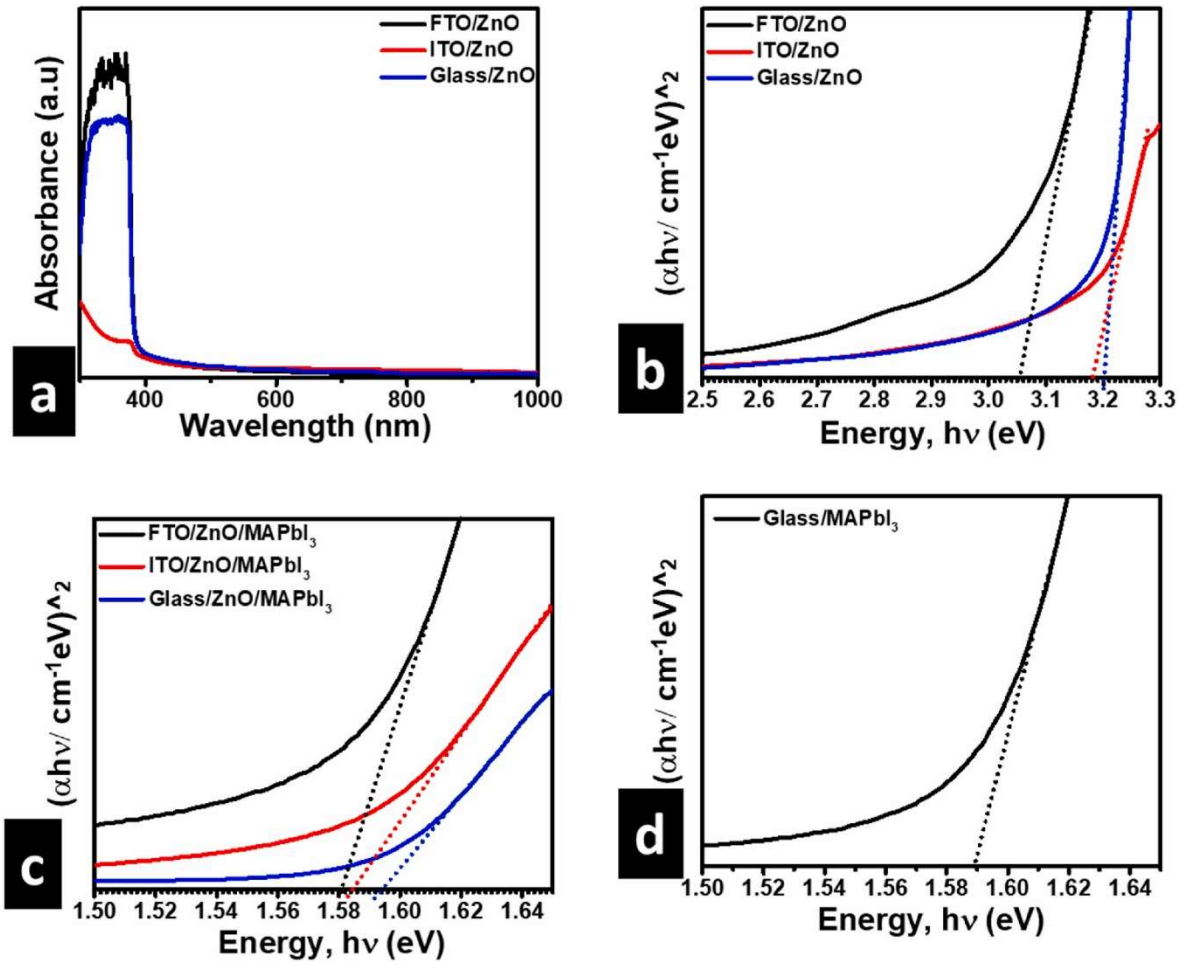

Fig. 8. (a) Absorption spectrum of ZnO-NRs on FTO, ITO, and glass (b) Tauc-plot for the absorption spectrum of ZnO-NRs on FTO, ITO, and glass (c) Tauc-plot for the absorption spectrum of $MAPbI_3$ thin film on FTO/ZnO, ITO/ZnO, and glass/ZnO and (d) Tauc-plot for the absorption spectrum of $MAPbI_3$ thin film on the glass.

The bandgaps were computed using the Mott and Davis relation given by **Eq.** 5,

$$(\alpha h\upsilon)^{\frac{1}{n}} = A\,(h\upsilon - E_g) \tag{5}$$

where E_g is bandgap and A is a proportionality constant, α is the absorption coefficient, h is the Planck's constant, υ is the frequency, n is a numerical constant, and its value determines the nature of the transition; n equals 1/2, 2, 3/2, and 3 for direct allowed transitions, indirectly allowed transitions, directly forbidden transitions, and indirect forbidden transitions respectively. Mott and Davis's equation shows that the optical absorption strength is proportional to the difference between photon energy and bandgap. A Plot of the absorption strength against photon energy is known as the Tauc's plot and is used to determine the bandgap of semiconductors. Fig. 8(a-d) shows Tauc's plots for ZnO and $MAPbI_3$ direct bandgap materials on the various substrates. We observe in Fig. 8(b) that the bandgap of ZnO-NRs depends on the substrate type. The bandgap of ZnO-NRs is 3.05, 3.18, and 3.20 eV on FTO, ITO, and glass substrates, respectively. These values are in close agreement with previous reports [35,39]. Fig. 8 (d) shows the Tauc-plot of the absorption spectrum of $MAPbI_3$ thin film on the glass. The horizontal intercept on Fig. 8 (d) is slightly different from the intercepts on Fig. 8(c). This shows that the bandgap of $MAPbI_3$ varies with the substrate. Fig. 9(a) shows a negative correlation between bandgap and average crystallite size of ZnO-

NRs on FTO, ITO, and glass substrates. The correlation between bandgap and crystallinity of ZnO-NRs has previously been observed by *Benramache* et al. [40]. Our results suggest that one can tune the crystallinity and bandgap of ZnO-NRs by changing the substrates and that the NRs on FTO are more crystalline and have a lower bandgap than those on ITO. Fig. 9(b) shows a weak inverse relationship between the bandgap and diameter of NRs, indicating a less significant quantum confinement effect. Significant quantum confinement exists in ZnO-NRs for diameters less than 10 nm, and the quantum confinement can be transferred from colloidal solutions to thin films [41,42]. For the $MAPbI_3$ thin film on ZnO-NRs grown on various substrates, the relationship between the crystallite size and the bandgap is different from that observed for the ZnO-NRs on the same substrates. Here, the bandgaps and crystallinity of $MAPbI_3$ on FTO/ZnO and ITO/ZnO are very different from that of $MAPbI_3$ on glass/ZnO with no evident linear relationship between bandgap and crystallinity, as shown in Fig. 9(c). Fig. 9 (d) shows bandgap vs. average grain size of $MAPbI_3$ on FTO/ZnO, ITO/ZnO, and glass/ZnO. We observed that the bandgap of $MAPbI_3$ varies with substrate and decreases with increase in average grain size.

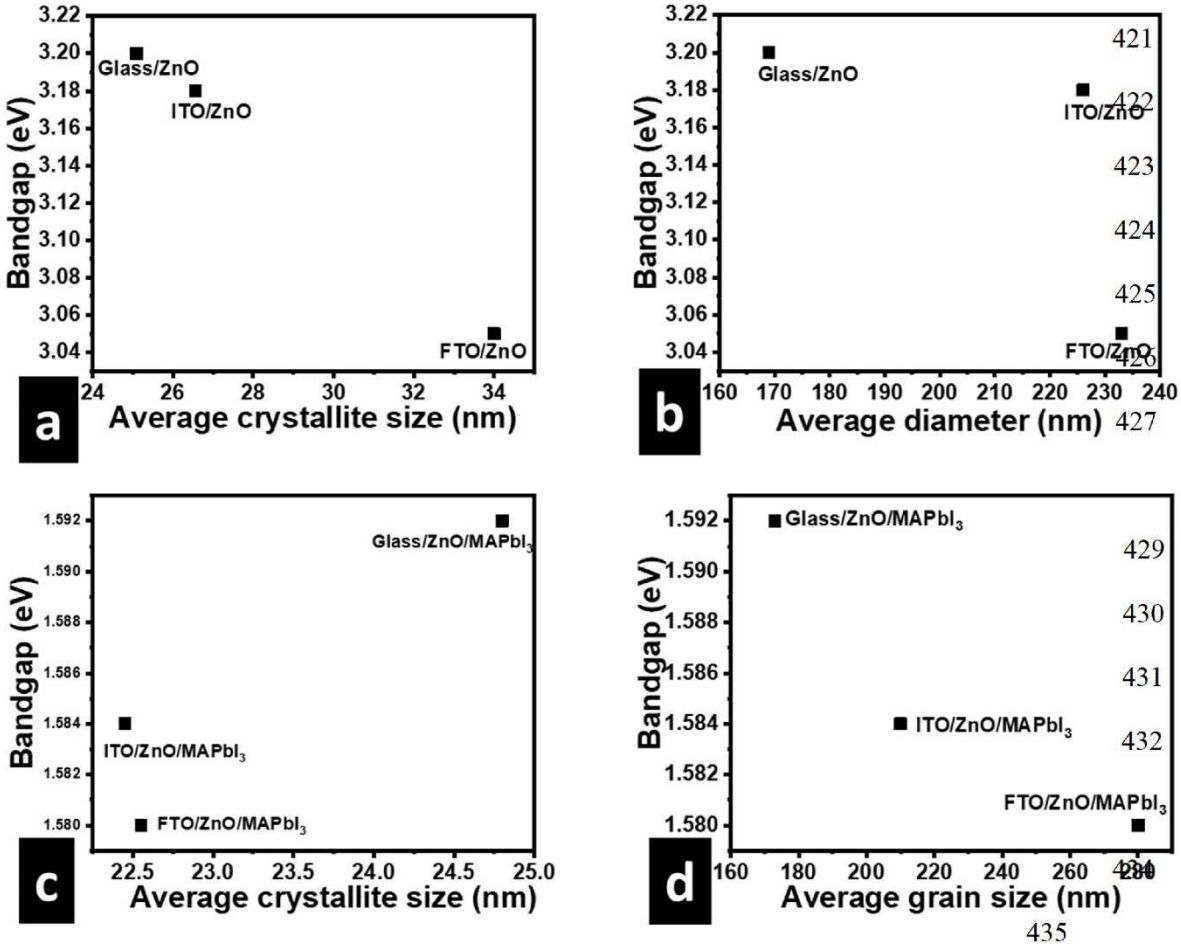

Fig. 9. (a) Bandgap vs. average crystallite size of ZnO-NRs on FTO, ITO, and glass (b) Bandgap vs. average diameter of ZnO-NRs on FTO, ITO, and glass (c) Bandgap vs. average crystallite size of $MAPbI_3$ on FTO/ZnO, ITO/ZnO, and glass/ZnO and (d) Bandgap vs. average grain size of $MAPbI_3$ on FTO/ZnO, ITO/ZnO, and glass/ZnO.

3.4. Electrical properties

Fig. 10 shows the semi-log dark current-voltage (*I–V*) plots of FTO/ZnO/Au,FTO/ZnO/ $MAPbI_3$/Au ITO/ZnO/$MAPbI_3$/Au, and ITO/ZnO/Au Schottky diodes. All devices were rectifying since the forward and reverse curves are anti-symmetric. This means that FTO/ZnO/Au and ITO/ZnO/Au serve as Schottky diodes, consistent with the literature [43]. Likewise, the FTO/ZnO/$MAPbI_3$/Au and ITO/ZnO/$MAPbI_3$/Au can function as photodiodes [44]. The current through the metal-semiconductor interfaces of the devices can be expressed by **Eq.** 6 [45],

$$I = I_s \exp\left[\frac{q(V-IR_s)}{nkT}\right]\left\{1-\exp\left(\frac{q(V-IR_s)}{kT}\right\}\right. \tag{6}$$

where R_8 is the series resistance, q is the electron charge, V is the forward-bias voltage, k is the Boltzmann constant, T is the absolute temperature, n is the ideality factor, and I_8 is the saturation current derived from the straight-line intercept of the Ln(V) versus V and is defined by Eq. (7) [46],

$$I_s = AA^*T^2 \exp\left(-\frac{qQ_{ap}}{kT}\right) \tag{7}$$

where A is the effective diode area, A^* is the effective Richardson constant, Q_{ap} is the apparent zero-bias barrier height. The ideality factor n can be obtained as in **Eq.** 8 [46],

$$n = \frac{q}{kT}\left(\frac{dV}{dLn(I)}\right) \tag{8}$$

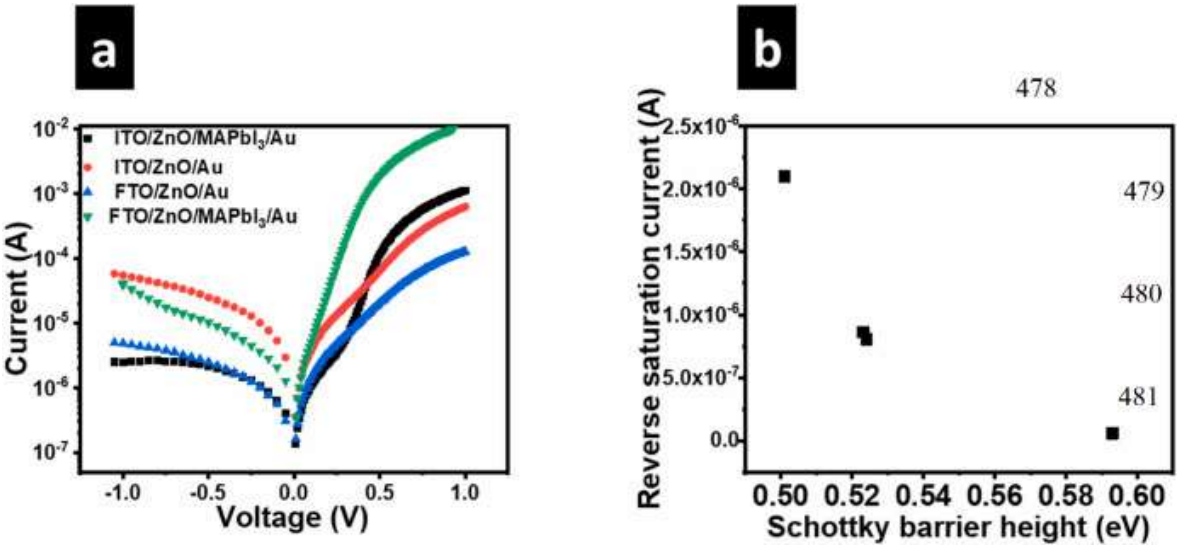

Fig. 10. (a) Semi-log plots of the dark I–V characteristics of FTO/ZnO/Au, FTO/ZnO/$MAPbI_3$/Au, ITO/ZnO/Au, and ITO/ZnO/$MAPbI_3$/Au Schottky diodes, and (b) Reverse saturation current vs. Schottky barrier height.

The zero-bias barrier height φ_{bh} was determined from the saturation current I_8. This was obtained at $V = 0$ V and is given by Ref. [46] **Eq.** 9,

$$\varphi_{bh} = \frac{kT}{q} Ln\left(\frac{AA^*T^2}{I_s}\right) \tag{9}$$

Using the above equations, the Schottky barrier height φ_{bh}, the ideality factor *n*, the series resistance Rs, and the reverse saturation current were calculated and shown in Table 3. Since the thickness of the $MAPbI_3$ thin film is less than 500 nm, the $MAPbI_3$ is fully depleted when forward bias, previously reported [[47], [48], [49]]. The full depletion of the thin $MAPbI_3$ film causes the FTO/ZnO/$MAPbI_3$/Au and ITO/ZnO/$MAPbI_3$/Au devices to behave more like FTO/ZnO/Au and ITO/ZnO/Au Schottky diodes under dark conditions, consistent with *Moeini* et al. [47]. The ideality factors were greater than 2, indicating high defect concentration and shunts that could lead to recombination and leakage currents, respectively [50]. However, we observed that significant differences occur in their ideality factors. The ideality factors for FTO/ZnO/$MAPbI_3$/Au and ITO/ZnO/$MAPbI_3$/Au are smaller compared to those for FTO/ZnO/Au and ITO/ZnO/Au. This suggests that FTO/ZnO/$MAPbI_3$/Au and ITO/ZnO/$MAPbI_3$/Au are better diodes. Both devices on FTO have smaller series resistance values, compared to the values on ITO. This could be due to the smaller resistance of the FTO substrate. Importantly, it is observed that FTO/ZnO/$MAPbI_3$/Au has the highest dark current in forward bias. The phenomenon is consistent with the smallest value of series resistance for the FTO/ZnO/$MAPbI_3$/Au device, as shown in Table 3. Although all devices were far from being ideal (with n as 1.0), the diode FTO/ZnO/$MAPbI_3$/Au showed the lowest ideality factor of 2.12. This indicates that FTO/ZnO/$MAPbI_3$/Au is the best of the four diodes. There is an inverse correlation between reverse saturation current and Schottky barrier height, as shown in Fig. 10(b). This inverse dependence is consistent with **Eq.** 9, indicating a larger Schottky barrier height is required to reduce the leakage current.

Table 3. Dark I–V parameters of ITO/ZnO/$MAPbI_3$/Au and FTO/ZnO/$MAPbI_3$/Au Schottky diodes at room temperature.

Samples	ideality factor, *n*	Saturation current, I_s (A)	Schottky barrier height Φ_{ev} (eV)	Series resistance, R_s (Ω)
ITO/ZnO/Au	5.361	2.10×10^{-6}	0.501	291.638
ITO/ZnO/$MAPbI_3$/Au	2.556	5.65×10^{-8}	0.593	227.845
FTO/ZnO/Au	5.783	8.63×10^{-7}	0.523	172.39
FTO/ZnO/$MAPbI_3$/Au	2.118	8.02×10^{-7}	0.524	38.766

Fig. 11 shows the current density (*J*) against voltage (*V*) characteristic of illuminated FTO/ZnO/$MAPbI_3$/Au and ITO/ZnO/$MAPbI_3$/Au solar cells. Also presented in Table 4 are the performance parameters of solar cells under illumination. The PCE of the devices is lower than that of exiting state-of-the-art performing devices using ZnO electron transport layers [10]. The low performance of our devices could be due to structural defects (traps) in the perovskite and ZnO layers. These traps could lead to recombination losses within the device. Also, poor device performance could be caused by lower shunt resistance compared to those of high-performing solar cells. The shunt resistance values for high-performance perovskite solar cells are in the order of tens of kilo-ohms [51,52] However, our values are in hundreds of ohms. These lower values indicate the presence of shunting paths that lead to leakage currents in the device. The shapes of the curves for the fabricated devices are similar but with different intercepts, suggesting that short current density (J_{sc}) and open-circuit voltage (V_{oc}) depends on the nature of the substrates. The fill factor (FF) of the solar cells on FTO is 50.60% while that on ITO is 48.25%. The lower value of FF could be due to low shunt resistance (R_{sh}) and high series resistance (R_s), as shown in Table 4, consistent with the literature [53]. Recall that the resistance of the ITO (8–12 Ω/sq) is slightly greater than that of the FTO (∼7 Ω/sq). The higher resistance of the ITO substrate may contribute to the greater series resistance of the solar cell. The solar cells on the FTO substrate showed a higher PCE

when compared to similar devices on ITO, as shown in Table 4. This is consistent with the previous investigations including polymer solar cells [37]. This could be due to the lower series resistance and higher shunt resistance. Also, the Schottky diodes on FTO showed better quality (lower ideality factor) and lower series resistance than those on ITO. Thus, there exists a negative correlation between the quality of the diodes and the PCE of the solar cells with the series resistance. This could be because the resistivity of ITO increases when annealed above 300 °C while that of FTO does not show significant changes in properties after high-temperature annealing [37,54].

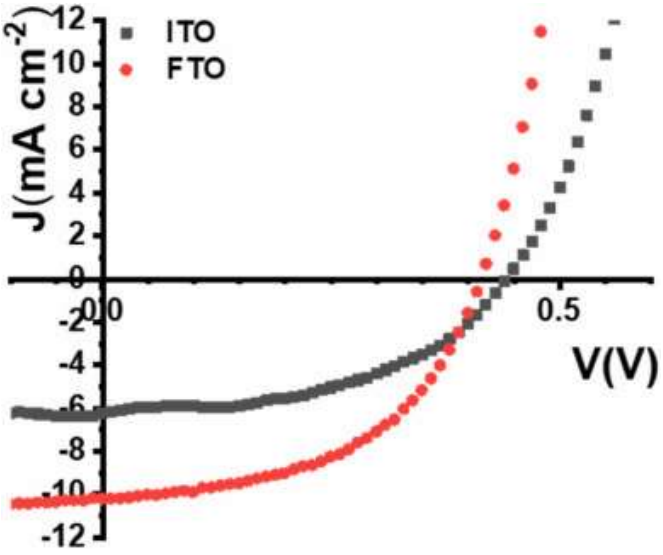

Fig. 11. J-V characteristics of ITO/ZnO/$MAPbI_3$/Au and FTO/ZnO/$MAPbI_3$/Au.

Table 4. Parameters of FTO/ZnO/$MAPbI_3$/Au and ITO/ZnO/$MAPbI_3$/Au hole transport layer-free solar cells under illumination.

	PCE (%)	FF (%)	J_{sc}(mA cm^{-2})	V_{oc} (V)	MP (W)	R_{sh} (Ω cm^2)	R_s (Ω cm^2)
Device on FTO sample	2.13	50.60	−10.20	0.41	−2.13	425.64	8.59
Device on ITO sample	1.32	48.25	−6.23	0.44	−1.32	177.50	17.50

4. Conclusions

In this work, ZnO-NRs were prepared on FTO, ITO, and microscopic glass substrates by chemical bath deposition. In-situ annealed $MAPbI_3$ perovskite was grown on the FTO/ZnO, ITO/ZnO, and glass/ZnO substrates by sequential physical vapor deposition. The structural, morphological, and optical properties of the NRs and $MAPbI_3$ were observed to vary on the different substrates. X-ray diffraction micrographs confirmed a pure (without PbI_2) tetragonal $MAPbI_3$ phase with I4/mcm space group and highly textured wurtzite hexagonal ZnO crystal structure, with the $P6_3mc$ space group. Unlike in one-step solution deposition of $MAPbI_3$ on ZnO that results in thermal decomposition during annealing, the pure $MAPbI_3$ films indicated that there was no thermal decomposition of $MAPbI_3$ to PbI_2 during in-situ annealing. This means that the sequential physical vapor deposition approach can be applied to grow $MAPbI_3$ films on ZnO without thermal decomposition. FE-SEM images revealed compact cuboidal $MAPbI_3$ grains on the ZnO-NRs. The average diameters of NRs were 233 ± 32, 226 ± 23, and 169 ± 35 nm on FTO, ITO, and glass substrates, respectively. Similarly, the respective average grain sizes of the $MAPbI_3$ thin films on FTO/ZnO, ITO/ZnO, and glass/ZnO

substrates were 280 ± 39, 210 ± 42, and 173 ± 19 nm. A comparison of the various NR diameters and corresponding average grain sizes of $MAPbI_3$ showed a positive correlation. UV–Vis absorption spectra revealed that FTO/ZnO absorbed more in the visible region than ITO/ZnO. The bandgaps of the NRs were 3.05, 3.18, and 3.20 eV, and those of $MAPbI_3$ were 1.580, 1.584, and 1.592 eV on FTO, ITO, and glass substrates, respectively. We observed a negative correlation between bandgap and average crystallite size of ZnO-NRs on FTO, ITO, and glass substrates; an indication that the bandgap of ZnO-NRs decreases with increases in crystallinity. A slight non-linear drop in bandgap with an increase in the average diameter of NRs, saying that quantum confinement effects were insignificant. This less significant quantum confinement effect could be due to diameters exceeding the critical value of 10 nm. Similarly, the bandgap of $MAPbI_3$ showed an inverse dependence with average grain size. Analysis of dark current-voltage characteristics using pure thermionic emission model revealed that the ideality factors ITO/ZnO/$MAPbI_3$/Au and FTO/ZnO/$MAPbI_3$/Au Shottky diodes were two times smaller than that of ITO/ZnO/Au and ITO/ZnO/Au diodes, accordingly. Also, the series resistances of the Schottky device structures containing $MAPbI_3$ were much lower than corresponding devices without $MAPbI_3$, with FTO/ZnO/$MAPbI_3$/Au having the minimum series resistance of 38.766 Ω. An inverse correlation was observed between the reverse saturation current and the Shottky barrier height, as expected from thermionic emission theory calculations. Hole transport layer-free solar cells using FTO substrates showed a greater PCE and FF than the corresponding solar cells on ITO. This could be because the resistivity of ITO increases when annealed above 300 °C while that of FTO does not show significant changes in properties after high-temperature annealing. This is useful information for the sustainability and performance improvement of halide perovskite technology because indium is scarce and may deplete over time. Generally, we observed that the nature/property of an electrode has a significant impact on the structural, morphological, optical properties of ZnO-NRs and ZnO/$MAPbI_3$ layers, and the performance of ITO/ZnO/$MAPbI_3$/Au and FTO/ZnO/$MAPbI_3$/Au devices.

Author's statement

M. A. Mayimele: Conceptualization; writing; synthesis of ZnO NRs films and their UV–Vis, SEM characterization, and electrical measurements. Solar cell dark I–V measurements and analysis. **J. N. Fru**: Conceptualization; synthesis of $MAPbI_3$ films and their UV–Vis, SEM characterization, XRD characterization, analysis and interpretation of results; solar cell fabrication, characterization; and writing. **J. S. Nyarige:** Conceptualization; data analysis; writing. **M. Diale:** Supervision, and proofreading of the final manuscript.

Declaration of competing interest

All authors declare no conflict of interest.

Acknowledgments

The authors wish to thank the University of Pretoria; the National Research Foundation/The World Academy of Sciences (NRF-TWAS); NRF grant no N0115/115463 of the SARChI and the Externally Funded UP Post-Doctoral Fellowship Programme: Grant Cost Centre N0115/115463 of the SARChI financial support.

References

[1] P. Zhang, J. Wu, T. Zhang, Y. Wang, D. Liu, H. Chen, L. Ji, C. Liu, W. Ahmad, Z. D. Chen, S. Li, Perovskite solar cells with ZnO electron-transporting materials, *Adv. Mater.* 30 (2018) 1–20, https://doi.org/10.1002/adma.201703737.
[2] M. Mekhnache, A. Drici, L.S. Hamideche, H. Benzarouk, A. Amara, L. Cattin, J. C. Bernède, M. Guerioune, Properties of ZnO thin films deposited on glass, ITO and ZnO:Al substrates, Superlattice. *Microst*. 49 (2011) 510–518, https://doi.org/10.1016/j.spmi.2011.02.002.
[3] F. Solís-Pomar, E. Martínez, M.F. Melèndrez, E. Pèrez-Tijerina, Growth of vertically aligned ZnO nanorods using textured ZnO films, *Nanoscale Res. Lett*. 6 (2011) 1–11, https://doi.org/10.1186/1556-276X-6-524.
[4] A.A. hssi, L. Atourki, N. labchir, M. Ouafi, K. Abouabassi, A. Elfanaoui, A. Ihlal, K. Bouabid, Electrodeposition of oriented ZnO nanorods by two-steps potentiostatic electrolysis: effect of seed layer time, *Solid State Sci*. 104 (2020) 106207, https://doi.org/10.1016/j.solidstatesciences.2020.106207.
[5] J. Yang, B.D. Siempelkamp, E. Mosconi, F. De Angelis, T.L. Kelly, Origin of the thermal instability in CH3NH3PbI3 thin films deposited on ZnO, *Chem. Mater*. 27 (2015) 4229–4236, https://doi.org/10.1021/acs.chemmater.5b01598.
[6] Y. Cheng, Q.D. Yang, J. Xiao, Q. Xue, H.W. Li, Z. Guan, H.L. Yip, S.W. Tsang, Decomposition of organometal halide perovskite films on zinc oxide nanoparticles, *ACS Appl. Mater. Interfaces* 7 (2015) 19986–19993, https://doi.org/10.1021/acsami.5b04695.
[7] S.H. Ahmadi, M. Ghaffarkani, M. Ameri, N. Safari, E. Mohajerani, Solvent selection for fabrication of low temperature ZnO electron transport layer in perovskite solar cells, *Opt. Mater*. 106 (2020), https://doi.org/10.1016/j.optmat.2020.109977, 109977.
[8] S. Li, P. Zhang, H. Chen, Y. Wang, D. Liu, J. Wu, H. Sarvari, Z.D. Chen, Mesoporous PbI2 assisted growth of large perovskite grains for efficient perovskite solar cells based on ZnO nanorods, *J. Power Sources* 342 (2017) 990–997, https://doi.org/10.1016/j.jpowsour.2017.01.024.
[9] V. Consonni, J. Briscoe, E. K¨arber, X. Li, T. Cossuet, ZnO nanowires for solar cells: a comprehensive review, *Nanotechnology* 30 (2019), https://doi.org/10.1088/1361-6528/ab1f2e.
[10] Y. Sun, Y. Gao, J. Hu, C. Liu, Y. Sui, S. Lv, F. Wang, L. Yang, Comparison of effects of ZnO and TiO2 compact layer on performance of perovskite solar cells, *J. Solid State Chem*. 287 (2020) 121387, https://doi.org/10.1016/j.jssc.2020.121387.
[11] D. Son, J. Im, H. Kim, N. Park, 11% efficient perovskite solar cell based on ZnO nanorods: an effective charge collection system 118 (2014) 16567–16573, https://doi.org/10.1021/jp412407j.
[12] K. Sivashanmugan, C.H. Lin, S.H. Hsu, T.F. Guo, T.C. Wen, Interfacial engineering of ZnO surface modified with poly-vinylpyrrolidone and p-aminobenzoic acid for high-performance perovskite solar cells, *Mater. Chem. Phys*. 219 (2018) 90–95, https://doi.org/10.1016/j.matchemphys.2018.08.022.
[13] P.H. Joshi, L. Zhang, I.M. Hossain, H.A. Abbas, R. Kottokkaran, S.P. Nehra, M. Dhaka, M. Noack, V.L. Dalal, The physics of photon induced degradation of perovskite solar cells, *AIP Adv*. 6 (2016) 115114, https://doi.org/10.1063/1.4967817.
[14] M.M. Tavakoli, R. Tavakoli, Z. Nourbakhsh, A. Waleed, U.S. Virk, Z. Fan, High efficiency and stable perovskite solar cell using ZnO/rGO QDs as an electron transfer layer, *Adv. Mater. Interfaces* 3 (2016) 1–10, https://doi.org/10.1002/admi.201500790.
[15] J. Song, L. Liu, X.F. Wang, G. Chen, W. Tian, T. Miyasaka, Highly efficient and stable low-temperature processed ZnO solar cells with triple cation perovskite absorber, *J. Mater.*

Chem. A. 5 (2017) 13439–13447, https://doi.org/10.1039/c7ta03331a.
[16] H. Slimani, N. Bessous, S. Dagher, A. Hilal-Alnaqbi, M. El Gamal, B. Akhozheya, M. Mohammed, Growth of ZnO nanorods on FTO glass substrate, *Mater. Res. Express* 7 (2020), 025026, https://doi.org/10.1088/2053-1591/ab727b.
[17] S. Yun, T. Guo, Y. Li, X. Gao, A. Huang, L. Kang, Well-ordered vertically aligned ZnO nanorods arrays for high-performance perovskite solar cells, *Mater. Res. Bull*. 130 (2020) 110935, https://doi.org/10.1016/j.materresbull.2020.110935.
[18] Z.N. Urgessa, R. Ruess, S.R. Tankio Djiokap, J.R. Botha, D. Schlettwein, Effect of morphology and surface treatment on the performance of ZnO nanorod-based dye-sensitized solar cells, *J. Alloys Compd.* 798 (2019) 249–256, https://doi.org/10.1016/j.jallcom.2019.05.298.
[19] P. Dash, A. Manna, N.C. Mishra, S. Varma, Synthesis and characterization of aligned ZnO nanorods for visible light photocatalysis, *Phys. E Low-Dimensional Syst. Nanostructures*. 107 (2019) 38–46, https://doi.org/10.1016/j.physe.2018.11.007.
[20] Y. S ¸ahin, S. ¨Oztürk, N. Kilinç, A. K¨osemen, M. Erkovan, Z.Z. ¨Oztürk, Electrical conduction and NO2 gas sensing properties of ZnO nanorods, *Appl. Surf. Sci*. 303 (2014) 90–96, https://doi.org/10.1016/j.apsusc.2014.02.083.
[21] P. Hari, M. Baumer, W.D. Tennyson, L.A. Bumm, ZnO nanorod growth by chemical bath method*, J. Non-Cryst. Solids* 354 (2008) 2843–2848, https://doi.org/10.1016/j.jnoncrysol.2007.09.097.
[22] B.S. Mwankemwa, S. Akinkuade, K. Maabong, J.M. Nel, M. Diale, Effects of surface morphology on the optical and electrical properties of Schottky diodes of CBD deposited ZnO nanostructures, *Phys. B Condens. Matter* 535 (2018) 175–180, https://doi.org/10.1016/j.physb.2017.07.030.
[23] M.H. Kumar, N. Yantara, S. Dharani, M. Graetzel, S. Mhaisalkar, P. Boix, N. Mathews, ZnO-based perovskite solid state solar cells, *Chem Com*m 49 (2013) 11089–11091, https://doi.org/10.1039/c3cc46534a.
[24] J.N. Fru, N. Nombona, M. Diale, Characterization of sequential physical vapor deposited methylammonium lead tri-iodide perovskite thin films, *Vacuum* 182 (2020) 109727, https://doi.org/10.1016/j.vacuum.2020.109727.
[25] J.N. Fru, N. Nombona, M. Diale, Synthesis and characterisation of methylammonium lead tri-bromide perovskites thin films by sequential physical vapor deposition, *Phys. B Phys. Condens. Matter.* 578 (2020) 411884, https://doi.org/10.1016/j.physb.2019.411884.
[26] V.P. Dinesh, P. Biji, A. Ashok, S.K. Dhara, M. Kamruddin, A.K. Tyagi, B. Raj, Photocatalytic degradation of industrial textile dyes using hybrid ZnO @ Ag core–shell nanorods, *RSC Adv*. 4 (2014) 58930–58940, https://doi.org/10.1039/c4ra09405k.
[27] P.E. Gnerrex-Bnllnw, Effects of preferred orientation on X-ray diffraction patterns of gypsum, *Am. Mineral*. 60 (1975) 127–129.
[28] W. Wu, G. Hu, S. Cui, Y. Zhou, H. Wu, Epitaxy of vertical ZnO nanorod arrays on highly (001)-oriented ZnO seed monolayer by a hydrothermal route, *Cryst. Growth* Des. 8 (2008) 4014–4020, https://doi.org/10.1021/cg800210m.
[29] D. Shi, V. Adinolfi, R. Comin, M. Yuan, E. Alarousu, A. Buin, Y. Chen, S. Hoogland, A. Rothenberger, K. Katsiev, Y. Losovyj, X. Zhang, P.A. Dowben, O.F. Mohammed, E.H. Sargent, O.M. Bakr, Low trap-state density and long carrier diffusion in organolead trihalide perovskite single crystals, *Science* 347 (2015) 519–522, https://doi.org/DOI:10.1126/science.aaa2725.
[30] M.I. Saidaminov, A.L. Abdelhady, B. Murali, E. Alarousu, V.M. Burlakov, W. Peng, I. Dursun, L. Wang, Y. He, G. MacUlan, A. Goriely, T. Wu, O.F. Mohammed, O. M. Bakr, High-quality bulk hybrid perovskite single crystals within minutes by inverse temperature crystallization, *Nat. Commun*. 6 (2015) 1–6, https://doi.org/10.1038/ncomms8586.

[31] N.J. Jeon, J.H. Noh, Y.C. Kim, W.S. Yang, S. Ryu, S. Il Seok, inorganic–organic hybrid perovskite solar cells, *Nat. Mater.* 13 (2014) 897–903, https://doi.org/10.1038/NMAT4014.
[32] A. Jesche, M. Fix, A. Kreyssig, W.R. Meier, P.C. Canfield, X-ray diffraction on large single crystals using a powder diffractometer, *Philos. Mag. A* 96 (2016) 2115–2124, https://doi.org/10.1080/14786435.2016.1192725.
[33] A.L. Patterson, The Scherrer formula for X-ray particle size determination, *Phys. Rev.* 56 (1939) 978–982, https://doi.org/10.1103/PhysRev.56.978.
[34] A.R. Stokes, A.J.C. Wilson, The diffraction of X-rays by distorted crystal aggregates-I, *Proc. Phys. Soc*. 56 (1944) 174, https://doi.org/10.1088/0959-5309/56/3/303.
[35] A. S´aenz-Trevizo, P. Am´ezaga-Madrid, P. Piz´a-Ruiz, W. Antúnez-Flores, M. Miki-Yoshida, Optical band gap estimation of ZnO nanorods, *Mater. Res.* 19 (2016) 33–38, https://doi.org/10.1590/1980-5373-MR-2015-0612.
[36] F. Haug, J. Yum, C. Ballif, Organometallic halide perovskites: sharp optical absorption edge and its relation to photovoltaic performance, *J. Phys. Chem. Lett*. 5 (2014) 1035–1039, https://doi.org/10.1021/jz500279b.
[37] F. Li, C. Chen, F. Tan, C. Li, G. Yue, L. Shen, W. Zhang, Semitransparent inverted polymer solar cells employing a sol-gel-derived TiO2 electron-selective layer on FTO and MoO3/Ag/MoO3 transparent electrode, *Nanoscale Res. Lett*. 9 (2014) 1–5, https://doi.org/10.1186/1556-276X-9-579.
[38] M. Ouafi, B. Jaber, L. Atourki, R. Bekkari, L. Laânab, Improving UV stability of MAPbI3 perovskite thin films by bromide incorporation*, J. Alloys Compd*. 746 (2018) 391–398, https://doi.org/10.1016/j.jallcom.2018.02.240.
[39] N. Mufti, S. Maryam, A.A. Fibriyanti, R. Kurniawan, A. Fuad, A. Taufiq, Sunaryono, Morphological Modification and Analysis of ZnO Nanorods and Their Optical Properties and Polarization, *Scanning*, 2018, p. 2018, https://doi.org/10.1155/2018/6545803.
[40] S. Benramache, O. Belahssen, A. Arif, A. Guettaf, Optik A correlation for crystallite size of undoped ZnO thin film with the band gap energy – precursor molarity – substrate temperature, *Optik* 125 (2014) 1303–1306, https://doi.org/10.1016/j.ijleo.2013.08.015.
[41] Y. Sun, Understanding quantum confinement and ligand removal in solution-based ZnO thin films from highly stable nanocrystal ink, *J. Mater. Chem*. C 6 (2018) 9181–9190, https://doi.org/10.1039/c8tc01536h.
[42] Y. Gu, I.L. Kuskovsky, M. Yin, S.O. Brien, G.F. Neumark, Quantum confinement in ZnO nanorods, *Appl. Phys. Lett*. 85 (2004) 3833–3835, https://doi.org/10.1063/1.1811797.
[43] S.M. Faraz, M. Willander, Q. Wahab, Interface state density distribution in Au/n-ZnO nanorods Schottky diodes, *IOP Conf. Ser. Mater. Sci. Eng*. 34 (2012), https://doi.org/10.1088/1757-899X/34/1/012006.
[44] N. Hernandez-Como, G. Rivas-Montes, F.J. Hernandez-Cuevas, I. Mejia, J. E. Molinar-Solis, M. Aleman, Ultraviolet photodetectors based on low temperature processed ZnO/PEDOT:PSS Schottky barrier diodes, *Mater. Sci. Semicond. Process*. 37 (2015) 14–18, https://doi.org/10.1016/j.mssp.2014.12.063.
[45] D. Korucu, A. Turut, H. Efeoglu, Temperature dependent I–V characteristics of an Au/n-GaAs Schottky diode analyzed using Tung ' s model, *Phys. B Phys. Condens. Matter*. 414 (2013) 35–41, https://doi.org/10.1016/j.physb.2013.01.010.
[46] M.A. Mayimele, M. Diale, W. Mtangi, F.D. Auret, Materials Science in Semiconductor Processing Temperature-dependent current–voltage characteristics of Pd/ZnO Schottky barrier diodes and the determination of the Richardson constant, *Mater. Sci. Semicond. Process*. 34 (2015) 359–364, https://doi.org/10.1016/j.mssp.2015.02.018.
[47] I. Moeini, M. Ahmadpour, A. Mosavi, N. Alharbi, N.E. Gorji, Modeling the time-

dependent characteristics of perovskite solar cells, *Sol. Energy* 170 (2018) 969–973, https://doi.org/10.1016/j.solener.2018.05.082.
[48] P. Yadav, D. Prochowicz, M. Saliba, P.P. Boix, S.M. Zakeeruddin, M. Grätzel, Interfacial kinetics of efficient perovskite solar cells, *Crystals* 7 (2017) 252, https://doi.org/10.3390/cryst7080252.
[49] J.N. Fru, N. Nombona, M. Diale, Characterization of thin MAPb(I1–xBrx)3 alloy halide perovskite films prepared by sequential physical vapor deposition*, Front. Energy Res*. 9 (2021), https://doi.org/10.3389/fenrg.2021.667323.
[50] O. Breitenstein, J. Bauer, P.P. Altermatt, K. Ramspeck, Influence of defects on solar cell characteristics*, Solid State Phenom*. 156 (2009) 1–10, https://doi.org/10.4028/www.scientific.net/SSP.156-158.1.
[51] R. Singh, S. Sandhu, J.J. Lee, Elucidating the effect of shunt losses on the performance of mesoporous perovskite solar cells, *Sol. Energy* 193 (2019) 956–961, https://doi.org/10.1016/j.solener.2019.10.018.
[52] Z. Bi, S. Zhang, M. Thandapani, Y. Zhu, Y. Zheng, N.Q. Liem, X. Xiao, G. Xu, A. Guerrero, X. Xu, High shunt resistance SnO2 -PbO electron transport layer for perovskite solar cells used in low lighting applications, *Adv. Sustain. Syst*. (2021) 2100120, https://doi.org/10.1002/adsu.202100120.
[53] N. Wu, Y. Wu, D. Walter, H. Shen, T. Duong, D. Grant, C. Barugkin, X. Fu, J. Peng, T. White, K. Catchpole, K. Weber, Identifying the cause of voltage and fill factor losses in perovskite solar cells by using luminescence measurements, *Energy Technol*. 5 (2017) 1827–1835, https://doi.org/10.1002/ente.201700374.
[54] A. Ahmadi, M.Z. Shoushtari, M. Farbod, Photoelectrochemical application of WS2 nanosheets prepared via a low-temperature CVD method *J. Mater. Sci. Mater. Electron*., 30 (2019), pp. 6342-6349, 10.1007/s10854-019-00936-7